

Numerical and experimental investigation of delaminations in a unidirectional composite plate using NDT and SHM techniques

Journal of Intelligent Material Systems and Structures
1–19

© The Author(s) 2020

Article reuse guidelines:

sagepub.com/journals-permissions

DOI: 10.1177/1045389X20978294

journals.sagepub.com/home/jim



Asaad Migot¹ , Hanfei Mei²  and Victor Giurgiutiu²

Abstract

In this paper, the non-destructive testing (NDT), structural health monitoring (SHM), and scanning laser Doppler vibrometer (SLDV) techniques were presented to quantify three simulated delaminations inserted at different depths of a unidirectional composite plate. First, the RollerFORM and Omniscan equipment were sufficiently used to identify the delaminations. Second, in conjunction with guided waves, the developed imaging method was successfully used to detect and quantify the interested delaminations. The tuning curves were determined experimentally to define the dominant Lamb wave modes of incident waves. Third, multi-physics three-dimensional finite element simulations of propagating and interacting Lamb waves with delaminations were implemented to extract the wavefield data for wavenumber analysis. The experimental part was conducted to validate the numerical results using SLDV. The effect of the delamination depth on the trapped waves generated over the delamination region was studied numerically and experimentally. The results showed that trapped waves could be affected by the delamination depth. Both numerical and experimental results demonstrated that the near surface delamination has strong trapped waves over the delamination region while the far surface delamination has weak trapped waves. The energy distribution maps of numerical and experimental wavefields data sufficiently quantified the interested delaminations. A good agreement was achieved between the numerical and experimental results.

Keywords

Structural health monitoring, non-destructive testing, composite materials, wave propagation, imaging methods, scattered waves, finite element simulation, wavenumber analysis

1. Introduction

1.1. State of the art

The advantages of the mechanical properties of composite materials have contributed to the development of aerospace structures. These materials have excellent mechanical properties and lightweight compared with metallic materials (Giurgiutiu, 2014; Migot et al., 2020). Different kinds of damage can occur in composite structures, such as delamination, matrix crack, and disbonding (Mei and Giurgiutiu, 2019a). These defects may be induced during manufacturing or by external impact and aging. They may grow and subsequently cause structural failure. Delamination represents the most invisible dangerous structural damage, leading to a catastrophic accident (Zou et al., 2000). The development and design of efficient structural health monitoring (SHM) techniques for successfully detecting and quantifying delamination is an argant demand. The

anisotropic behavior of composite materials makes the process of detecting damage more difficult compared with metallic materials (Gomes et al., 2018; Mei and Giurgiutiu, 2018). In recent years, various types of non-destructive testing (NDT) techniques have been developed and used to identify the structural damage such as ultrasonic testing, radiographic testing, electromagnetic testing, etc. (He and Hutchinson, 1989; He et al., 2017). However, NDT methods are much expensive and need more experience. The increasing use of aerospace and naval vehicles worldwide has made

¹Quality Assurance Department, Thi-Qar University, Nasiriyah, Iraq

²Department of Mechanical Engineering, University of South Carolina, Columbia, SC, USA

Corresponding author:

Asaad Migot, Quality Assurance Department, Thi-Qar University, Almsfawih Street, Nasiriyah 64001, Iraq.
Email: migotasaad@gmail.com

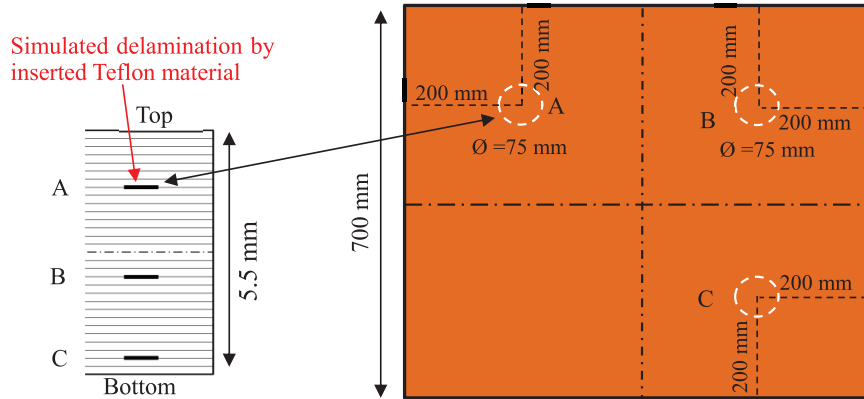


Figure 1. Schematic of the 5.5 mm unidirectional $[0]_{30}$ CFRP composite plate with three delaminations of the same sizes at various depths.

structural health monitoring (SHM) field an attractive scope for many researchers. The development of SHM techniques opens a perfect domain for using cheap, reliable, and effective monitoring systems by installing integrated sensors and analyzing the recorded data (Mei et al., 2016; Su et al., 2006). Many recent research works have approved the ability of SHM techniques for detecting and quantifying structural damage such as delamination. The SHM techniques, which include guided waves-based method, acoustic emission method, and electromechanical impedance (EMI) have been successfully used to detect delamination in composite structures (Michaels and Michaels, 2007; Migot et al., 2019; Park et al., 2014). Understanding the interaction of guided waves with damage is the key to the development of SHM techniques. Ultrasonic guided wave techniques have been widely used and demonstrated as a useful tool for structural health monitoring because of its sensitivity for damage detection and monitoring large area (Giurgiutiu and Soutis, 2012; Mei et al., 2019b). Piezoelectric wafer active sensors (PWAS) have been developed as cheap and lightweight sensors. These sensors can be easily installed on an interesting structure to generate and receive Lamb waves for SHM applications (Mei and Giurgiutiu, 2019b; Migot and Giurgiutiu, 2017). The FEM simulation provides a good tool for studying and analyzing guided wave interaction with different kinds of structural damage. It makes the design and development of SHM tools more easily (Mei et al., 2019a; Shen and Cesnik, 2016). The Lamb waves propagating in a composite plate are dispersive. Their velocities depend on the plate thickness, the frequency of excitation signal, and the fiber direction and laminate layup configurations (Hayashi and Kawashima, 2002). In recent years, many works have been implemented using guided waves for damage detection and localization in isotropic and composite materials (Azuara et al., 2018; Haider et al., 2018; Ihn and Chang, 2008). The analysis of Lamb waves

interaction with damage could potentially detect, localize, and estimate the size of various kinds of damage in investigated structures. The wavefield data measured by a scanning laser Doppler vibrometer (SLDV) was analyzed using different methods to detect structural damage. Local wavenumber analysis approach was used for damage quantification in isotropic or composite plates (Mesnil et al., 2014; Tian et al., 2013). Manufacturing defects in a composite structure were identified using wavefield imaging method (Juarez and Leckey, 2016).

1.2. Scope of the article

This paper presents three NDT, SHM, and SLDV techniques to quantify three simulated delaminations' location and size in a unidirectional composite plate. We used the RollerFORM equipment to scan the areas of interest and identify the location and size of delaminations. We conducted experimental investigations to estimate the delamination size by using Lamb waves-based imaging methods. A numerical study using Multi-physics three-dimensional (3D) finite element (FE) simulation was implemented to visualize the interaction of the guided waves with delaminations. The numerical results were validated experimentally by implementing SLDV experiments. The numerical and experimental wavefields data were analyzed using local wavenumber analysis, and wavefield energy distribution maps to study the effect of delamination depth on the scattered and trapped waves and identify the shape, size, and location delaminations.

2. Unidirectional composite specimen

The specimen is a 5.5-mm-thick in-house unidirectional CFRP composite plate with a stacking sequence of $[0]_{30}$. The configuration of the unidirectional composite plate is given in Figure 1. The dimensions of the

Table 1. Engineering constants of the unidirectional prepreg (Mei et al., 2019a).

E_{11}	E_{22}	E_{33}	ν_{12}	ν_{13}	ν_{23}	G_{12}	G_{13}	G_{23}	ρ
140.8 GPa	11.3 GPa	11.3 GPa	0.31	0.31	0.5	5.7 GPa	5.7 GPa	3.4 GPa	1640 kg/m ³

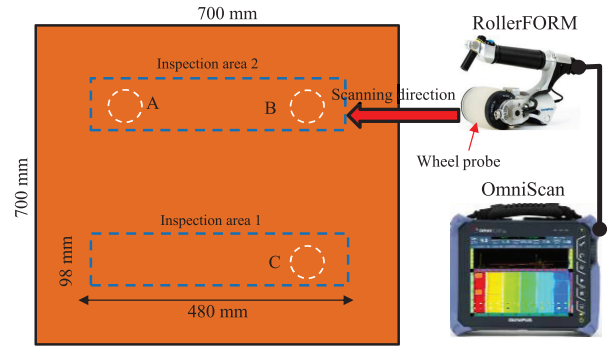
specimen were 700 mm \times 700 mm \times 5.5 mm. This specimen has three simulated delaminations inserted at different depths across the plate thickness created by inserting three circular Teflon films of the same size (75 mm in diameter) before curing in the autoclave. Delamination A (near the top surface) was generated between plies 7 and 8. Similarly, delamination B (near the mid-plane) was generated between plies 18 and 19, and delamination C (near the bottom surface) was made between plies 28 and 29, as shown in Figure 1. The material properties, given in Table 1, were measured experimentally using the ultrasonic immersion technique described in reference (Mei et al., 2019a).

3. NDT technique

Ultrasonic non-destructive testing (NDT) was performed on the unidirectional composite plate. The purpose of NDT is to detect and verify the simulated delaminations.

3.1. Experimental setup of NDT detection

The Olympus RollerFORM is a new phased array wheel probe design for zero-degree C-scan inspection of aerospace composite, aluminum panels, and similar components. We can use this tool for thickness measurement, material loss, detection and sizing of delamination and internal porosity. The RollerFORM scanner is a new phased array probe enclosed in a water chamber (RollerFORM Specifications, 2018). In this experiment, we employed a 3.5 MHz phased array probe to detect the delamination. The coverage width of the probe is approximately 49 mm. Therefore, a large inspection area can be divided into several areas scan. The width of each area scan is 49 mm. The experimental setup of the NDT detection on the composite plates is shown in Figure 2. The tire chamber should fill with Distilled deionized water a day before inspection to allow the water to degas completely. The OmniScan device should be set up for the RollerFORM wheel probe inspection. The RollerFORM wheel probe should be completely wet using a light water spray. We can inspect the whole or part of the interested area. For the 5.5-mm thick unidirectional [0]₃₀ CFRP composite plate, we conducted two inspection areas of the same size (480 mm \times 98 mm). The first inspection area only includes delamination C (near the bottom surface). In

**Figure 2.** Experimental set-up of NDT technique for scanning the composite specimen.

contrast, the second inspection area has delamination A (near the top surface) and delamination B (near the mid-plane).

3.2. NDT results

The NDT results of all inspection areas are shown in Figure 3. The C-scan image of the first inspection area shows that the circular delamination C has a light blue color map, which means this delamination is close to the bottom surface. The section view on delamination C (B-scan) demonstrated that delamination C is near the bottom surface. The C-scan image of the second inspection area on the unidirectional [0]₃₀ CFRP composite plate shows two same size circular delaminations, which are B and A. In this C-scan image, we can observe two circles with different color maps, which means delaminations B and A have different depths. The B-scan images of these delaminations indicate their depths across the plate thickness. The section view on delaminations B and A (B-scan images) demonstrated that delamination B is near the mid-thickness of the interesting specimen, and A is at the center of the upper half thickness. The A-scan plots show strong reflected signals from the upper and bottom surfaces. The reflected signals of delaminations have strong amplitudes. In contrast, the back-wall signals are very weak because the delamination blocked the phase array beam to hit the bottom surface of the plate. Based on these results, we can conclude that the sizes, shapes, and depths of these delaminations can be quantified from the NDT detection, which is consistent with the design.

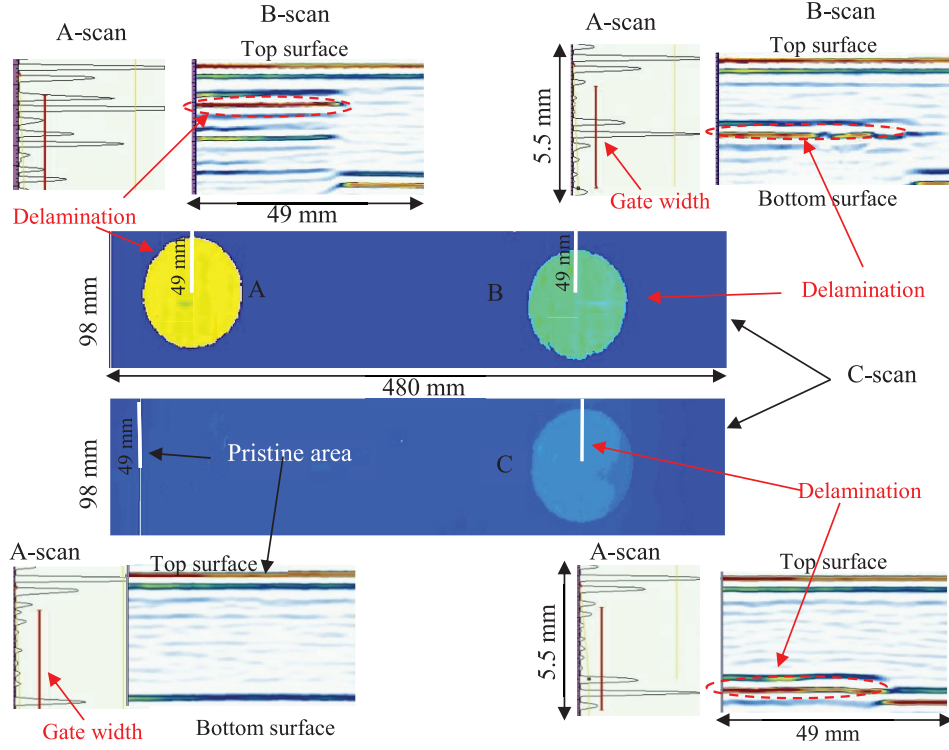


Figure 3. NDT results of the inspection areas on the unidirectional $[0]_{30}$ CFRP composite plate.

4. SHM technique for inspection test specimen

In this section, we used guided waves in conjunction with a developed imaging method to detect and quantify three simulated delaminations inserted at different depths of the unidirectional composite plate. In recent work (Haider et al., 2018; Mei et al., 2019b; Migot et al., 2019), improved imaging methods were developed to obtain accurate localization and sizing damage in metallic plates and composite laminates.

4.1. Principles of the imaging method

We implemented a developed imaging method to quantify the size and shape of damage in the composite plate. This method involved the Gaussian distribution function and scattering signals. The flowchart of the developed imaging method is illustrated in Figure 4. In this method, at first, the scattering signals were determined using the pitch-catch experimental modes. The interesting area was divided into pixels. The pitch-catch experimental mode involved elliptical orbit, and the TOF of every pixel can be determined using the following equation:

$$t_{ij} = \frac{\sqrt{(x_T - x_i)^2 + (y_T - y_j)^2}}{v_{g1}} + \frac{\sqrt{(x_i - x_R)^2 + (y_j - y_R)^2}}{v_{g2}} \quad (1)$$

where t_{ij} is TOF of scattered signal when the damage at pixel $p_{ij}(x, y)$; $x_T, y_T, x_R, y_R, x_i, y_j$ are the coordinates of transmitter sensor, receiver sensor, and pixel, respectively; and v_{g1}, v_{g2} are the group velocities of the incident path (the path from transmitter sensor to damage) and damage path (the path from damage to receiver sensor), respectively. The field value of each pixel is determined by using the Gaussian distribution function (Su et al., 2009). The equation of Gaussian distribution function (Migot et al., 2019) is:

$$f_{ij}^k(x, y) = \frac{1}{\sigma\sqrt{2\pi}} e^{-\frac{(x-\mu)^2}{2\sigma^2}} \quad (2)$$

where $f_{ij}^k(x, y)$ is the field value of every pixel $P_{ij}(x, y)$ of the image of a particular sensing path $T_m - R_n$ (transmitter T_m and receiver R_n), x representing the time of flight at each pixel point $t_{ij}(x, y)$ for the sensing path $T_m - R_n$, μ represents the time of flight of scattered wave packet for the sensing path $T_m - R_n$, which can be determined experimentally. The standard deviation, σ which describes the variability or dispersion of a data set, which was taken as half of the time range of wave packet.; m, n represents the index of transmitters and receivers, respectively, which vary from 1 to the total number of transmitters (N_T) and receivers (N_R), such as, $m = 1, 2, 3, \dots, N_T$ and $n = 1, 2, 3, \dots, N_R$. To fuse all the images of different sensing paths, the summation and/or multiplication algorithms were used following the equations below (Migot et al., 2019):

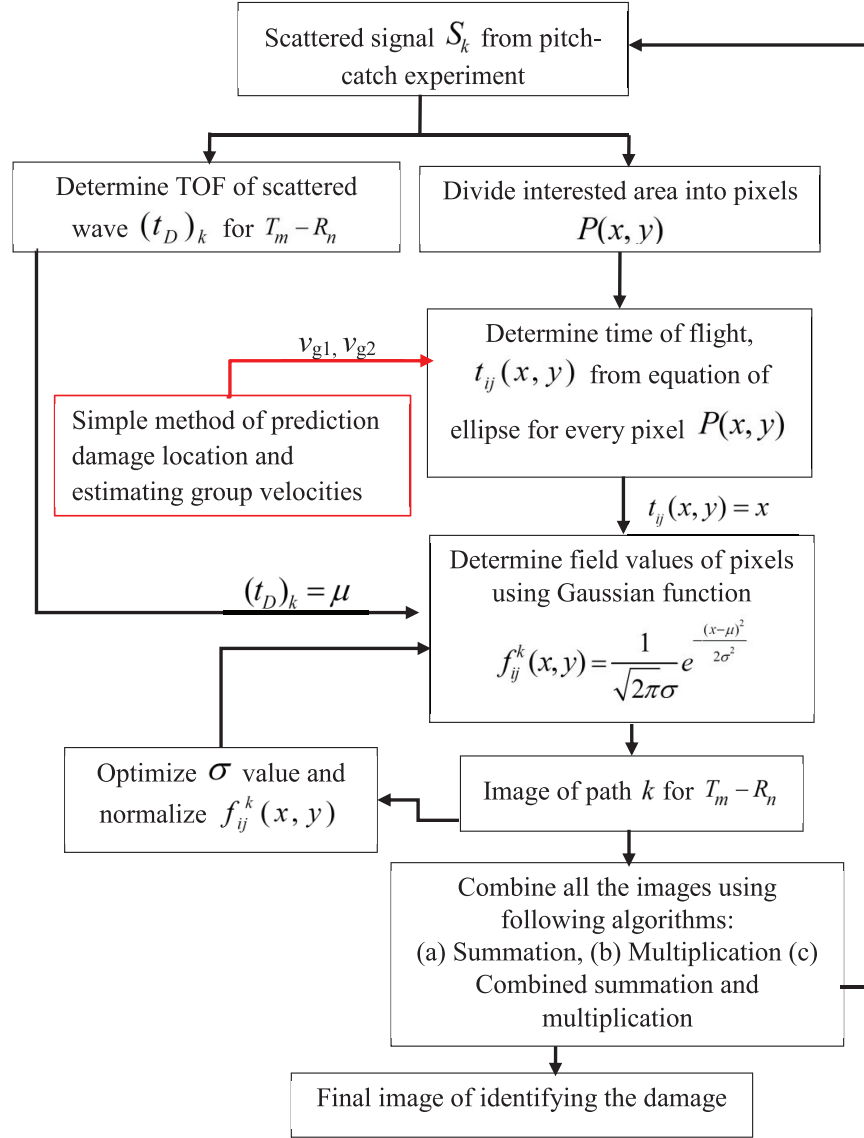


Figure 4. Flowchart of imaging method based on Gaussian distribution function. We added a new step of estimating the group velocity values to this flowchart.

$$\begin{aligned}
 P_{sum}(x, y) &= \sum_{k=1}^N f_{ij}^k(x, y) \\
 P_{mult}(x, y) &= \prod_{k=1}^N f_{ij}^k(x, y)
 \end{aligned} \quad (3)$$

where $P_{sum}(x, y)$, $P_{mult}(x, y)$ are the total field values of each pixel point using summation or multiplication algorithm; N represents the total number of sensing paths.

4.2. Experimental setup

The experimental setup of using the SHM technique to detect and quantify simulated delaminations in the test specimen is shown in Figure 5. We instrumented this specimen with a network of twenty-two PWAS

transducers on the bottom plate surface. These sensors have divided the specimen into four investigated areas. Three of them are damaged areas. The fourth one is the pristine area. The diameter of each PWAS transducer is 7 mm, and the thickness is 0.2 mm. The clay was applied to the plate edges to absorb boundary reflections. A function generator was used to generate three-count tone burst signals. The excitation frequency was swept from 20 to 500 kHz in steps of 15 kHz. An oscilloscope recorded the response signals.

4.3. Experimental tuning and dispersion curves

The tuning curves of Lamb modes propagating in a structural like plate have the priority to be studied to choose a useful dominant Lamb mode and appropriate

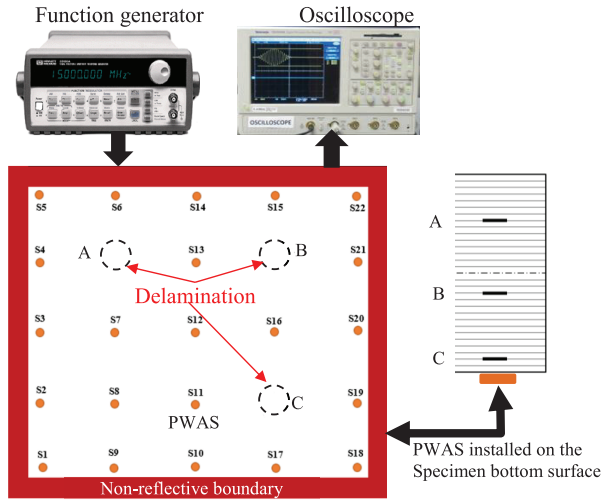


Figure 5. Experimental setup of the SHM technique on the unidirectional composite plate.

excitation signal frequency for investigating the interested area. This step is essential to better results of guided waves interaction with structural damage and gets strong scattered waves. The propagating Lamb wave modes (symmetric and antisymmetric modes) are dependent on the mechanical properties and the thickness of the interesting structure, and the excitation signal frequency (Yu and Giurgiutiu, 2010). In this work, we studied Lamb wave modes' tuning curves to detect better and quantify structural delamination. We conducted pitch-catch experiments for three sensing paths with different directions (fiber, transverse and 45° directions). In these experiments, the excitation signal frequency was swept from 20 to 500 kHz in steps of 15 kHz. Figure 6(a) shows the time domain signal at frequency 180 kHz of a sensing path in the fiber direction. The short-time Fourier transform (STFT) was performed on this signal to generate the time-frequency spectrum as shown in Figure 6(b). The analytical slowness curves obtained using the semi-analytical finite element (SAFE) method (Mei and Giurgiutiu, 2018) were superimposed with the time-frequency spectrum plot. We can observe that the signal energy is distributed among symmetrical Lamb mode (S0) and antisymmetric Lamb modes (A0 and A1). A time-domain signal at frequency 120 kHz in the transverse direction is shown in Figure 7(a). The signal energy is distributed among fundamental Lamb modes (A0 and S0) and shear horizontal guided wave (SH0), as shown in Figure 7(b). The SH0 appears due to the anisotropic behavior of composite materials in the off-axial direction (Giurgiutiu, 2018). Figure 8 shows the experimental tuning curves of three different propagating wave directions. Figure 8(a) shows the tuning curves in the fiber direction. We can notice that A1 is the dominant mode around a frequency of 300 kHz. For the

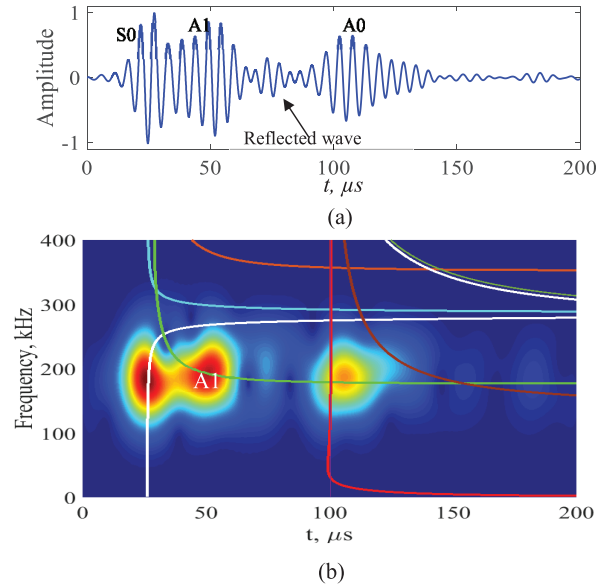


Figure 6. The pitch-catch signal of a sensing path in the fiber direction at center frequency 180 kHz: (a) signal time domain and (b) time-frequency spectrum combined with analytical slowness curves.

transverse and 45° directions, which are shown in Figure 8(b) and (c). We can observe that SH0 is the dominant mode around a frequency of 180 kHz. Based on tuning curves, we choose 300 kHz as an excitation signal frequency to excite incident guided waves in the fiber direction (0° direction) and 180 kHz as an excitation signal frequency to excite incident-guided waves transverse direction (90° direction) and 45° directions. We plotted experimental group velocity dispersion curves in the fiber and transverse directions for some Lamb wave modes. Figure 9 shows a good matching among the analytical and experimental group velocity dispersion curves in the fiber and transverse directions.

4.4. Experimental results

We conducted pulse-echo and pitch-catch experiments separately for every three damaged areas and the pristine area. For example, to investigate the interesting area of delamination C, the pulse-echo experiments were conducted for the PWAS S₁₆, S₁₇, S₁₁, and S₁₉ to detect and localize the damage using the proposed method in Section 4.1. Figure 10(a) shows the pulse-echo signals at frequency 300 kHz of the sensing paths S₁₆-S₁₆, S₁₇-S₁₇, S₁₁-S₁₁, and S₁₉-S₁₉. We can indicate that the scattered waves received by sensors S₁₆, S₁₇ have the same TOF values, and the scattered waves received by sensors S₁₁, S₁₉ also have the same TOF values. Hence, the damage is located at the center of the interesting area, as illustrated in Figure 10(b). After this step, we can determine the direction of the incident and scattered waves of a particular sensing path. The

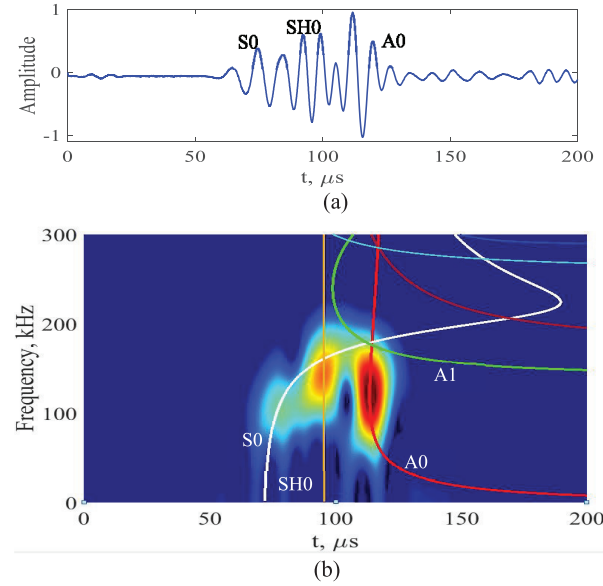


Figure 7. The pitch-catch signal of a sensing path in the transverse direction at center frequency 120 kHz: (a) signal time domain and (b) time-frequency spectrum combined with analytical slowness curves.

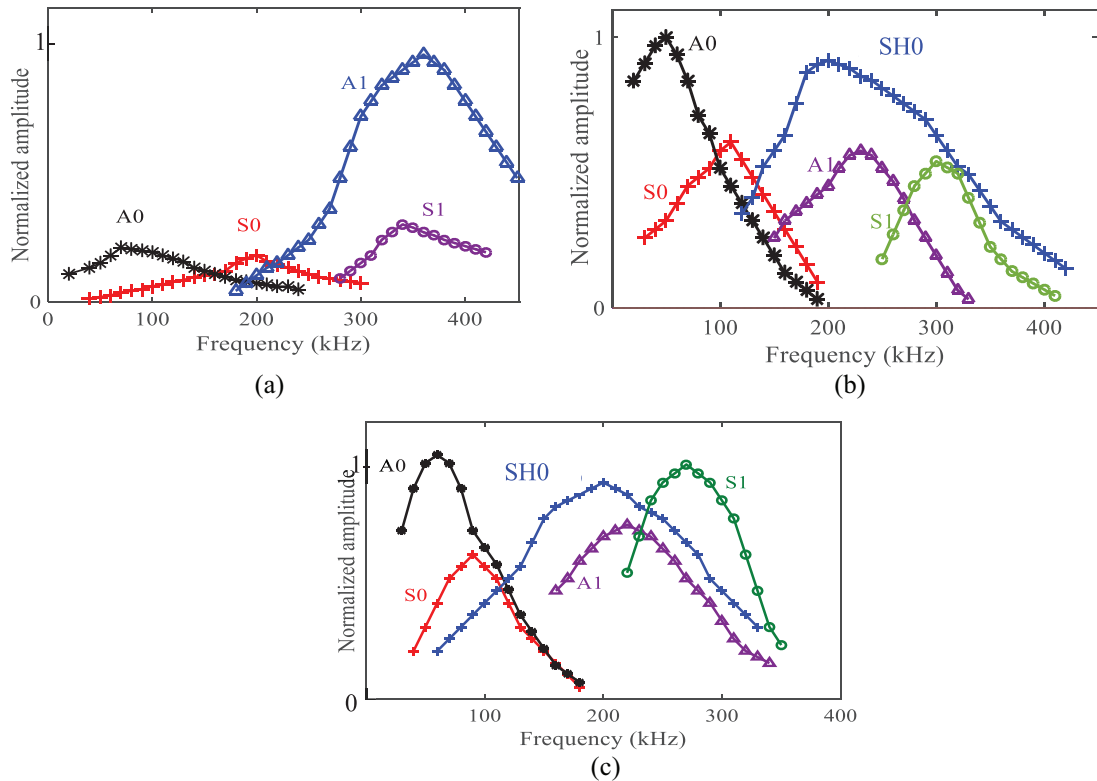


Figure 8. Experimental tuning curves of Lamb wave modes propagating in 5.5-mm unidirectional composite laminate with three different directions: (a) fiber direction (0°), (b) transverse direction (90°), and (c) 45° direction.

effect of delamination depth on the scattered waves can be observed. Figure 11 shows a comparison of three sensing paths signals of delaminated areas C, B, A, and a baseline signal. We have compared baseline signals of

three damaged cases, and they have consistent amplitudes. The scattered waves generated by delamination C (sensing path S_{18} - S_{19}) are more potent than other scattered waves generated by delamination B and A.

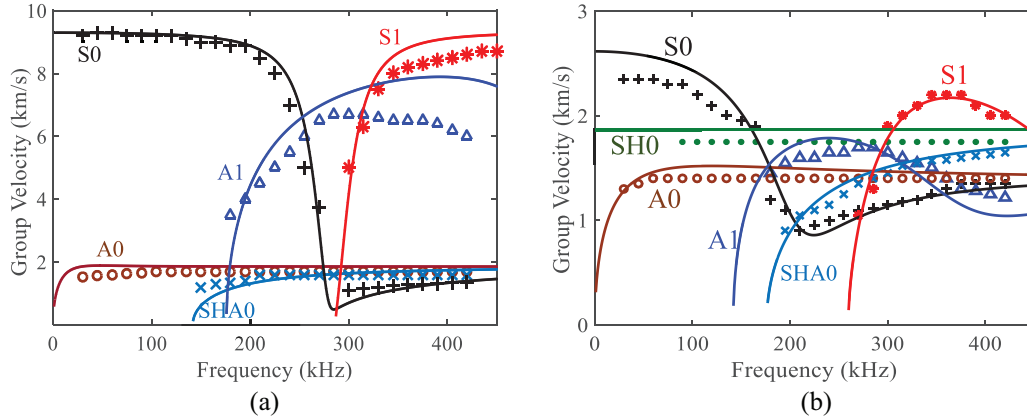


Figure 9. Experimental and analytical dispersion curves of Lamb wave modes propagating in 5.5-mm unidirectional composite laminate for two different directions: (a) fiber direction (0°) and (b) transverse direction (90°).

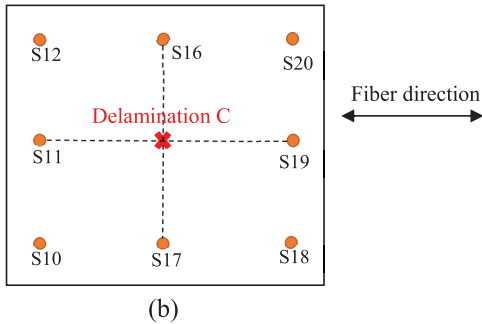
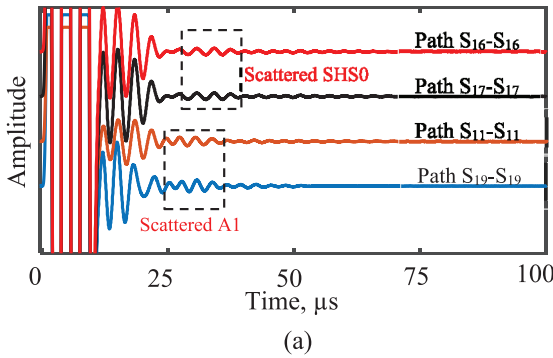


Figure 10. The new methodology of localizing a damage point: (a) pulse-echo signals at frequency 300 kHz received by four sensors around investigated area C and (b) predicting the location of delamination C.

We can say that the near-surface delamination has strong scattered waves compared with the far surface delamination.

After indicating the location of delaminations, we implemented pitch-catch experiments for all three damaged and pristine areas. Each damaged area has a network of eight sensors. Each sensor network element acted as a transmitter to generate guided waves, whereas the rest of the eight sensors acted as receivers to capture the propagating guided waves. The experimental Lamb wave signals captured by different

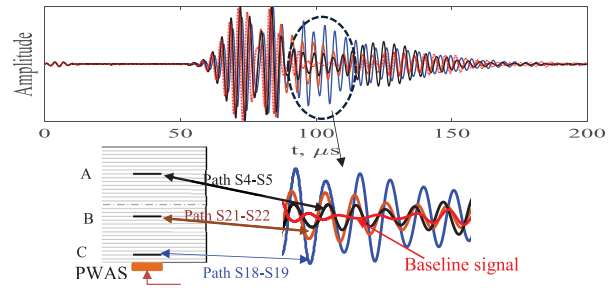


Figure 11. The effect of delamination depth on the scattering wave amplitude.

sensing paths were analyzed and compared with baseline signals to catch scattered waves generated after the interaction of Lamb waves with delaminations. Three delamination signals from selected sensing paths and three pristine signals are shown in Figure 12. Figure 12(a) shows pristine and measured signals in the fiber direction. The measured signals are transmitted by sensor S_{16} and received by sensor S_{12} . We can observe that symmetric Lamb wave S_0 is the dominant mode at frequency 180 kHz, which agrees with the experimental tuning curve of S_0 in the fiber direction. The SH_0 scattered wave observed in this sensing path signal can be approved by calculating the time of flight (TOF) of an incident path (transmitter to damage) and damage path (damage to a receiver) using corresponding distances and group velocity values. Figure 12(b) shows the delamination signals in the transverse direction at frequency 300 kHz (sensing path S_{11} - S_{12}). We can identify the dominant modes SH_0 and S_1 by overlapping the FFT spectrum with slowness curves in the transverse direction. The SH_0 scattered wave can be observed. The pristine signal and delamination signal, the signal of sensing path S_6 - S_{13} , in 45° direction, can be seen in Figure 12(c). The dominant modes of S_1 and SH_0 were identified by overlapping the FFT spectrum with

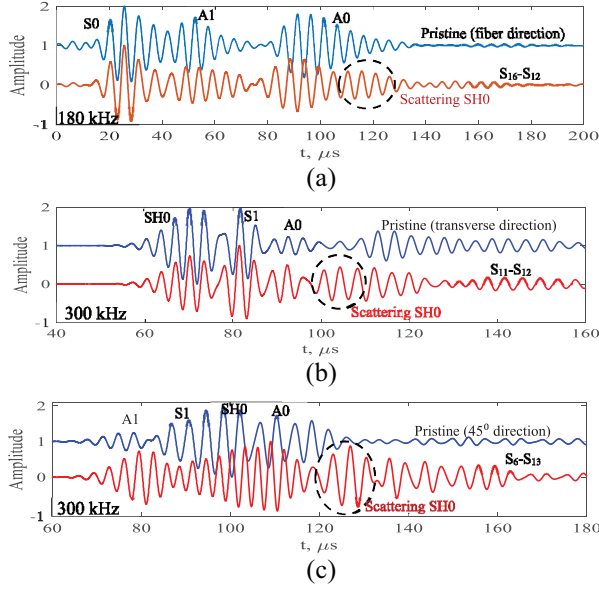


Figure 12. Pristine and measured signals of three sensing paths in different directions: (a) fiber direction, (b) transverse direction, and (c) 45° direction.

slowness curves. We can easily observe SH0 scattered waves. The TOF of SH0 scattered wave for a particular sensing path was determined to use it with the developed imaging method in the next steps of localizing and quantifying the delamination, as illustrated in the flowchart of Figure 4. Based on the imaging method, the investigated area is divided into small pixels. The TOF is determined at every pixel of a particular sensing image using equation (1). Figure 13 shows three cases of determining TOF of scattered waves based on the configuration of sensing paths. In these cases, we can observe the Lamb modes of the incident and scattered waves. The field value of every pixel of the image of a particular sensing path can be determined using equation (2). To determine the size and location of the delaminations, the sensing paths of multiple transmitters of each investigated area were used to get multiple

intersection points representing the delamination edges. A new methodology using a combination of summation and multiplication algorithms has been developed to visualize the delamination without a threshold setting. In the first step of this methodology, we have used the summation algorithm (Wang et al., 2004) to extract the individual images of all the sensing paths for each PWAS transmitter. These images have strong intersection points (pixels with high field values), representing the delamination edges, and the rest are undesirable orbits (pixels with small field values). The second step aims to keep strong intersection points of damage edges by increasing the field values of pixels with the damage edges and removing undesirable orbits by decreasing field values of pixels with undesirable trajectories. We have used the multiplication algorithm (Michaels and Michaels, 2007) to fuse all of these individual images of the first step to obtain the final image of visualizing delamination, which does not require a threshold setting. Figure 14(a) shows the final imaging result of quantifying three delaminations using the imaging summation algorithm with a threshold value (about 80% of maximum field value). We can observe four strong spots around each delamination, which represent its edges. The final image can be constructed without setting threshold value using combined of summation and multiplication algorithms, as illustrated in Figure 14(b). The edges of each delamination can be observed. Both imaging results match well with the real delaminations.

5. Guided waves–delamination interaction: Numerical and experimental studies

Many efforts have been achieved using guided wave-field data measured by a scanning laser Doppler vibrometer (SLDV) to detect and quantify the damage. The wavefield data can be further analyzed for quantifying damage through frequency-wavenumber analysis, wavefield amplitude profile, and wavenumber imaging methods (Michaels et al., 2011; Ruzzene, 2007; Tian

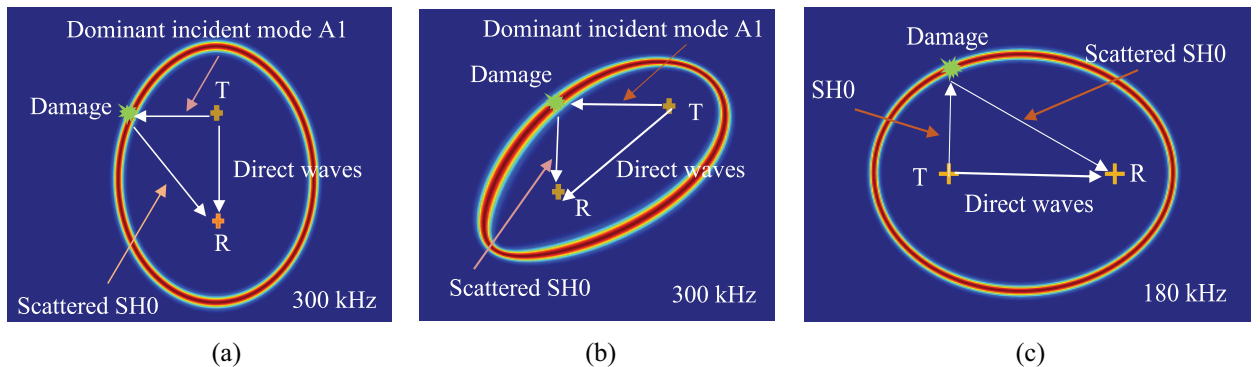


Figure 13 Three different cases of determining the TOF of scattering waves for three different directions of sensing paths: (a) transverse direction, (b) 45° direction, and (c) fiber direction.

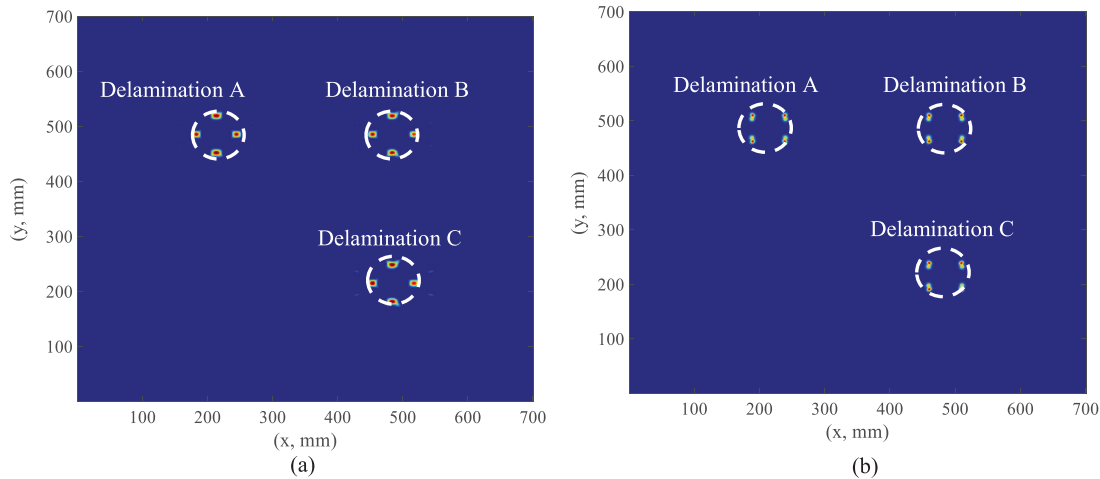


Figure 14. Imaging results of identifying the location and size of three simulated delaminations: (a) using summation algorithm and the set threshold value (80% of maximum threshold value) and (b) using a combined of summation and multiplication algorithms without sitting threshold value.

et al., 2015). In this section, the guided waves propagating and interaction with delamination was studied numerically using multi-physics finite element (FE) simulation and experimentally using SLDV. The wave-field data measured numerically and experimentally were analyzed to detect and size simulated delaminations and study the effect of delamination depth on the energy of generated trapped waves over the delamination region.

5.1. Multiphysics finite element simulation

Three sets of 3D simulations were carried out to investigate guided wave interaction with three simulated delaminations: (1) delamination A; (2) delamination B; (3) delamination C. Figure 15 shows the FE models of the unidirectional CFRP composite plate with three different delamination cases. In this study, the delaminations were modeled by detaching the nodes. For the case of delamination A, 75-mm delamination is created between layers 7 and 8 by specifying the delamination as two planes, which are defined by the same coordinates but are not tied together. For the case of delamination B, 75-mm delamination between plies 18 and 19 is generated. Finally, 75-mm delamination between plies 28 and 29 is introduced for the case of delamination C, as shown in Figure 15. These delamination depths were chosen based on the manufactured specimen in section 2. Non-reflective boundaries (NRB) can eliminate boundary reflections and thus allow for the simulation of guided wave propagation in an infinite medium with small-size models (Shen and Giurgiutiu, 2015). This NRB was implemented around the 3D FE models to calculate the transient response under the PWAS excitation. The PWAS transducer was modeled with coupled field elements (SOLID5) in ANSYS.

Structural solid elements (SOLID185) were used to mesh the composite plate. COMBIN14 spring-damper elements were utilized to construct the NRB. This study used a three-count Hanning window modulated tone burst with the center frequency of 120 kHz as the excitation signal.

5.2. Finite element results

The FE simulation of Lamb waves propagation and interaction with delamination C, B, and A can be observed in Figure 16. From this Figure, we can conclude that a significant interaction of guided waves with delamination can be affected by delamination depth. The symmetric Lamb wave mode (S0) has a weak interaction with delamination because of its low amplitude. The high amplitude of asymmetric Lamb wave mode (A0) makes a strong wave-damage interaction. We can notice a significant interaction of asymmetric Lamb wave mode (A0) with delamination C because it is close to the bottom surface, as shown the Figure 16(a). We can see weak Lamb waves-delamination interactions in Figure 16(b) and (c) because these delaminations (case B and case A) are far from the scanning surface (bottom surface). However, the interaction of delamination B with guided waves is slightly stronger than delamination A. The interaction of A0 with the delamination generates strong trapped waves over the delamination region. These trapped waves can be used to identify the shape, size, and location of the investigated delamination.

The simulated trapped waves over three delamination regions can be noticed in Figure 17. The delamination depth can significantly affect the energy of trapped waves over the delamination region. The delamination C has strong and intensive trapped waves over the

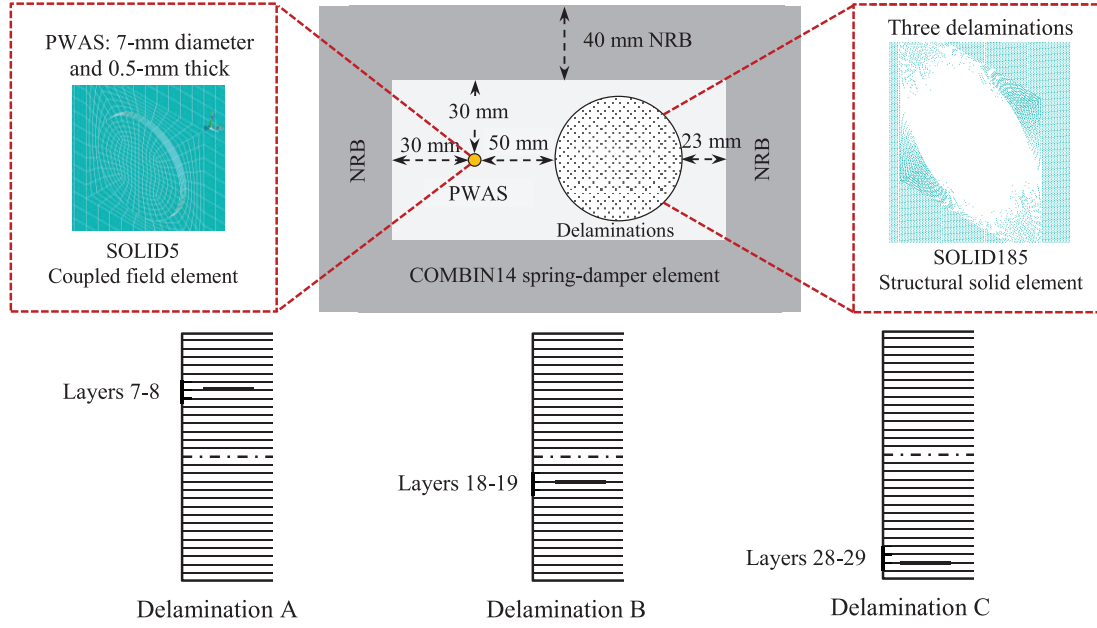


Figure 15. Multi-physics finite element model of the unidirectional composite plate with three different delamination cases.

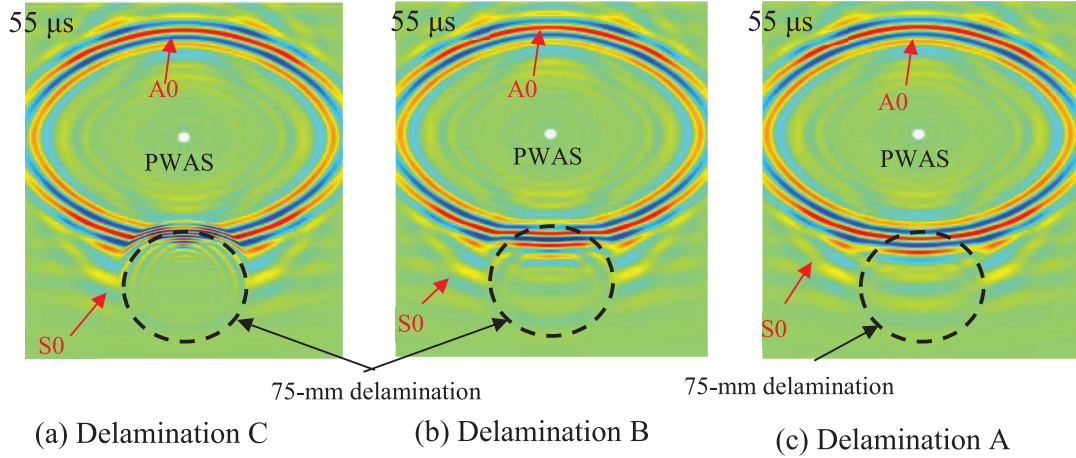


Figure 16. FE-measured wavefields at 55 μ s of three scanning areas at frequency 120 kHz: (a) scanning area C, (b) scanning area B, and (c) scanning area A.

delamination region because it is close to the scanning surface, as shown in Figure 17(a). The density and energy of trapped waves decrease with increasing the delamination depth, as observed in Figure 17(b) for delamination B and Figure 17(c) for delamination A. The trapped waves over delamination A are weaker than trapped waves over delamination C and slightly weaker than delamination B.

The energy distribution of the wavefields of scanning areas can be estimated to visualize and quantify the delaminations. The wavefield energy distribution was determined at each spatial point of a scanning area based on the root mean square (RMS) value (Radzieński et al., 2020):

$$E(x, y) = \sqrt{\sum_{n=1}^N [S_n(x, y)]^2} \quad (4)$$

where $E(x, y)$ represents the energy value at each spatial point of the scanning area; N is the total number of sample points; S_n is the amplitude value at each sample point. Figure 18 shows the energy distribution maps of numerical wavefields of scanning areas C, B, and A. The sizes of the three delaminations can be estimated. The delamination C was visualized because it has strong trapped waves over the delamination region. The clarity of visualizing delamination is decreased with increasing delamination depth, as

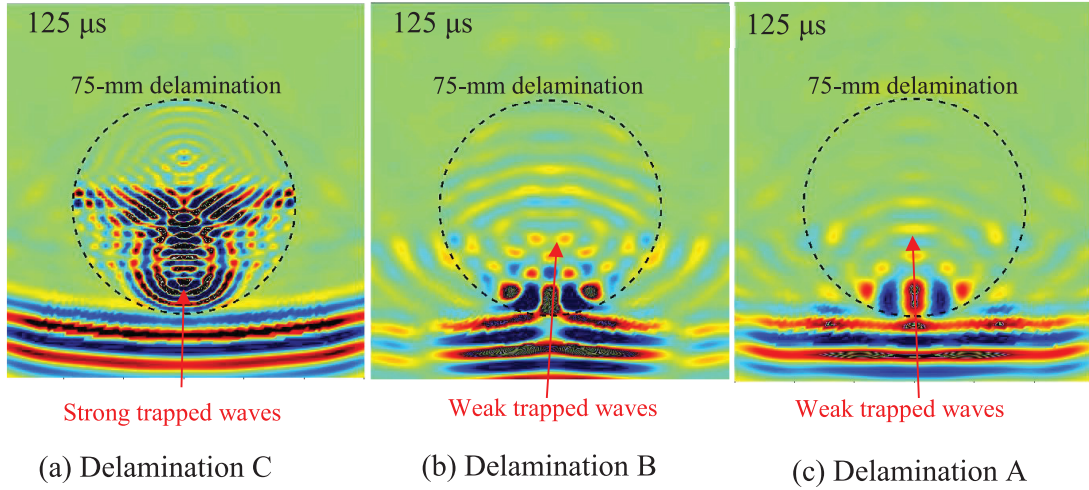


Figure 17. FE-measured trapped waves over three delamination regions at 125 μ s: (a) delamination C, (b) delamination B, and (c) delamination A.

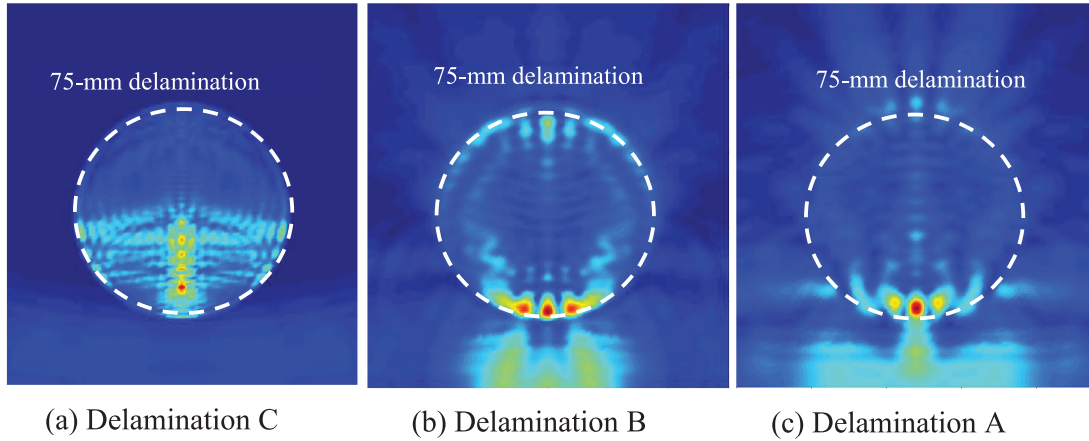


Figure 18. Energy distribution maps of the numerical wavefields of three scanning areas: (a) scanning area C, (b) scanning area B, and (c) scanning area A.

shown in Figure 18(b) for delamination B and Figure 18(c) for delamination A. Further signals analysis was implemented for the FE-wavefield data to study the effect of delamination depth on the interaction between guided waves and the delamination.

The time-space wavefield and corresponding frequency-wavenumber domain were obtained numerically for three lines of scan data across delaminations C, B, and A, as shown in Figure 19. Figure 19(a), (c), and (e) show the time-space wavefields of cases C, B, and A, respectively. We can notice two Lamb modes A0 and S0. The significant interaction and strong trapped waves can be observed in delamination C compared with delaminations B and A. The trapped waves over delamination B are slightly more robust than the trapped waves over delamination A. The corresponding frequency-wavenumber domains can be determined by

transforming the time-space wavefield using a two-dimensional fast Fourier transform. Figure 19(b), (d), and (f) show the wavenumber spectrums of delamination C, B, and A, respectively. We can observe that the positive wavenumber spectrums of incident A0 and S0 match well with analytical positive wavenumber curves of A0 and S0 modes. Because the delamination C is near the scanning surface, new strong wavenumber components on the positive side (forward propagation) and negative side (backward propagation) can be observed. For delaminations, B and A, new weak positive and negative wavenumber components can be observed because they are far from the scanning surface and have weak interactions with Lamb waves. The wavenumber components of delamination B are slightly more potent than delamination A as shown in Figure 19(d) and (f).

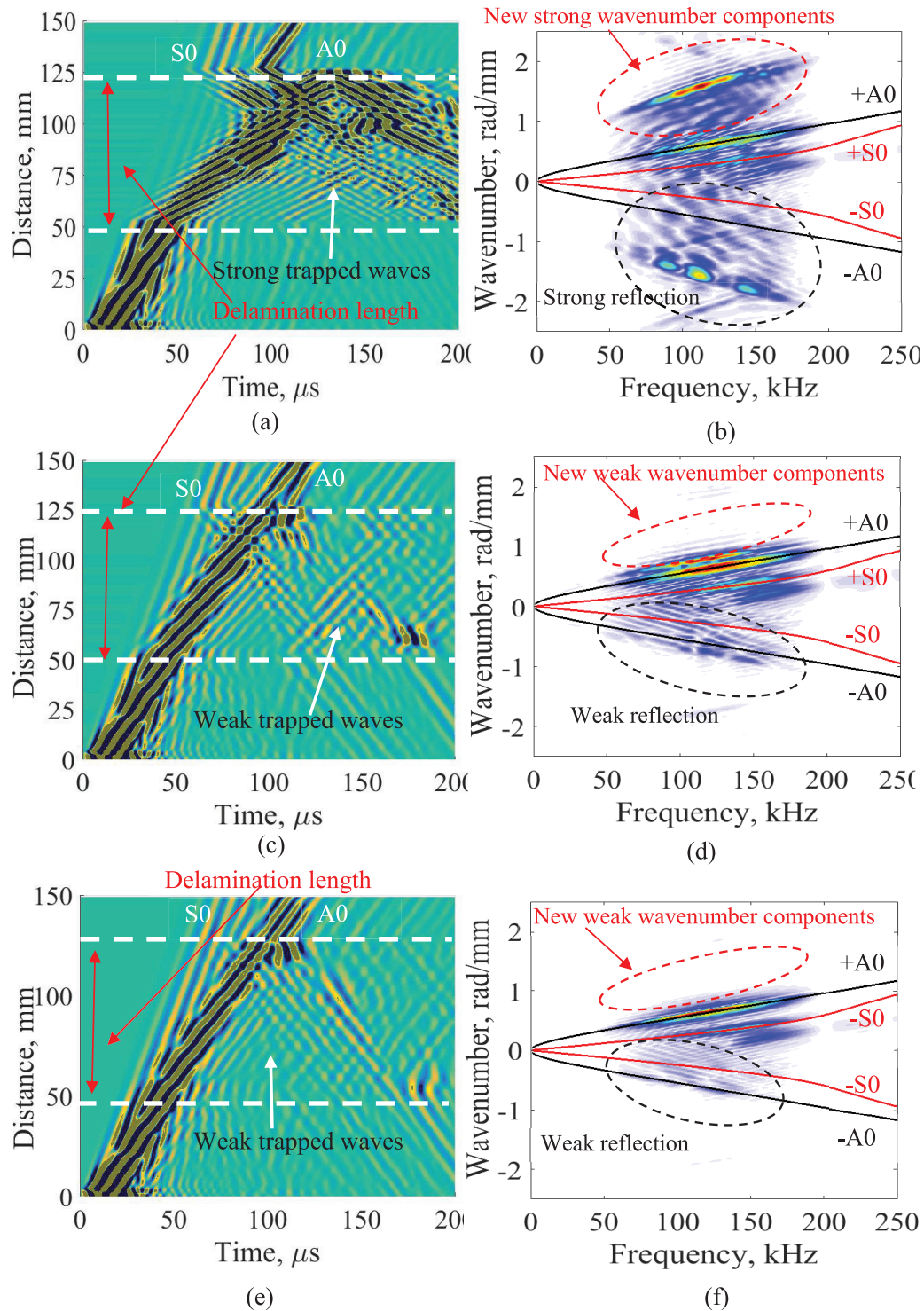


Figure 19. FE time-space wavefield and frequency-wavenumber spectrum of three delamination cases: (a and b) for delamination C, (c and d) for delamination B, and (e and f) for delamination A.

5.3. Experimental validations setup

The numerical results in the previous section will be validated experimentally by using scanning Laser Doppler vibrometer (SLDV). The guided wave interaction with delaminations can be visualized

experimentally using the hybrid PWAS transducer-SLDV. The experimental setup of SLDV is shown in Figure 20. In this experiment, the PWAS transducers were installed on the bottom surface of the test specimen to excite guided waves. The function generator

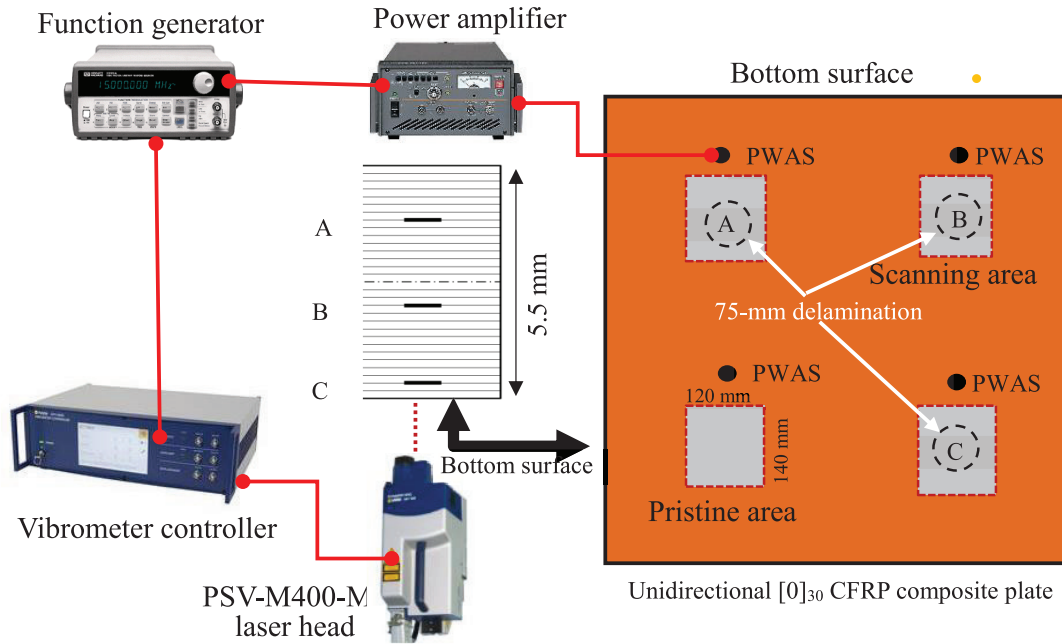


Figure 20. Experimental setup on the unidirectional $[0]_{30}$ CFRP composite plate using the SLDV measurement.

was used to generate a three-count tone burst signal with the center frequency of 120 kHz, which was amplified to 120 Vpp by the power amplifier. The amplifier applied to the PWAS transducer to excite the guided waves. The SLDV was used to acquire the time-space wavefields over the scanning lines and areas. The laser head generated a laser beam perpendicular to the scanning area (bottom surface of the investigated plate) to measure out of plan motion. We scanned three damaged and pristine areas in this experiment. These areas were covered with reflective taps to improve the surface and enhance the signal quality. The wavefield data of scanning lines and scanning areas can be analyzed to quantify the delaminations.

5.4. Experimental validations results

The SLDV can be used to acquire time-space data for every point of the scanning area. Every spatial point of the scanning area has a time-domain signal. These signals of spatial points can be used to extract wavefield images at a specific time. Figure 21(a) to (c) shows the experimental transient wavefield images for delamination areas C, B, and A, respectively. At time 55 μ s, we can observe two Lamb modes S_0 and A_0 propagating in the transverse direction in all three cases. The S_0 mode is weaker and slightly faster than A_0 mode. The S_0 generated weak interaction with the delaminations. The delamination C has a somewhat obvious interaction with S_0 compared with the other two delaminations, which matches well with FE results. After the interaction of A_0 mode with delaminations (specifically at time 125 μ s), trapped waves can be observed in the

three delaminations regions. The delamination C, which is near the scanning surface, has intensive and strong trapped waves over the delamination region. These trapped waves can be used to identify the location, size, and shape of delamination. As the delamination depth increases (case B and case A), the generated trapped waves over delamination regions, which are shown in Figure 21(b) and (c) respectively, become weak and less intensive as demonstrated it numerically in Figure 17. Based on numerical and experimental results, we can conclude that the delamination depth can affect the energy of trapped waves over the delamination region.

Figure 22 shows three experimental wavefield energy distribution maps of area C, B, and A. We can remark that scanning area C has strong energy distribution over the delamination region compared with area B, which is slightly stronger than area A. Based on the experimental wavefield energy distribution maps, the delamination C, B, and A can be quantified. Good agreements were achieved between the numerical (Figure 17) and experimental energy distribution maps of these three delaminations. The wavenumber analysis was used to analyze the experimental wavefield data to validate it with the FE result. The SLDV lines scan across the pristine and three damaged areas were conducted. For every line scan data, we obtained the time-space wavefield and corresponding frequency-wavenumber spectrum. The frequency wavenumber-spectrum can be determined experimentally by transforming the experimental time-space wavefield using two-dimensional fast Fourier transform. Figure 23 shows the time-space wavefield and corresponding frequency-wavenumber spectrum obtained from

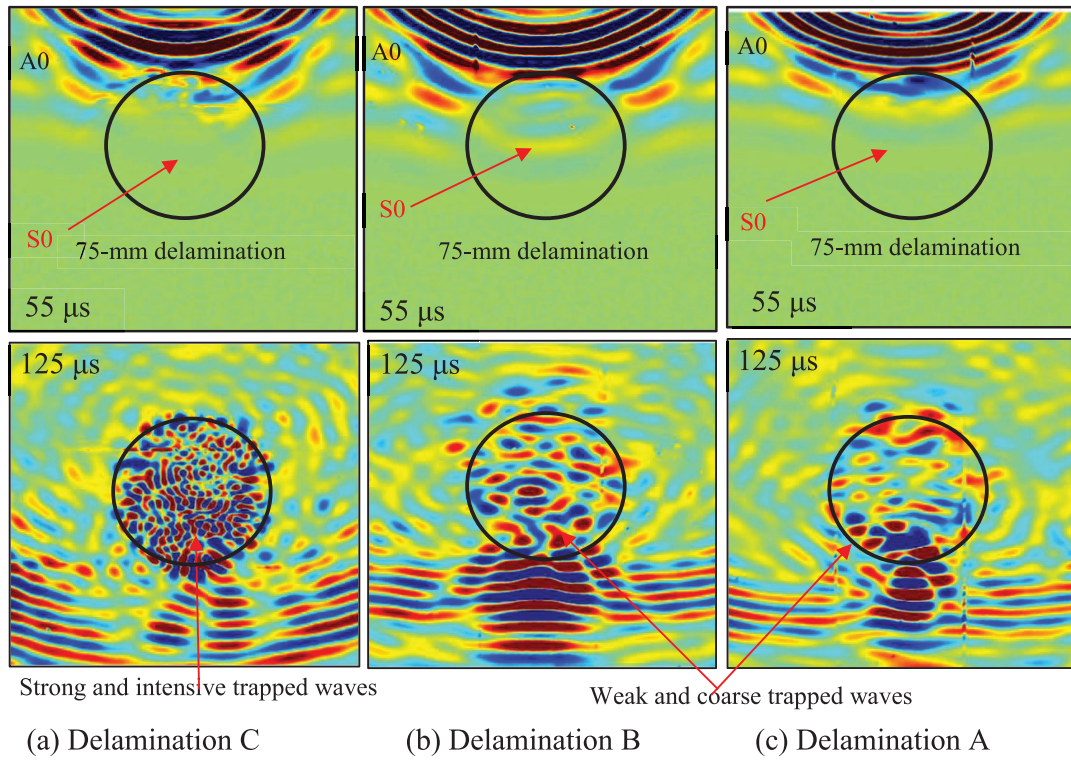


Figure 21. Experimental measured wavefields at certain times of three scanning areas at frequency 120 kHz: (a) scanning area C, (b) scanning area B, and (c) scanning area A.

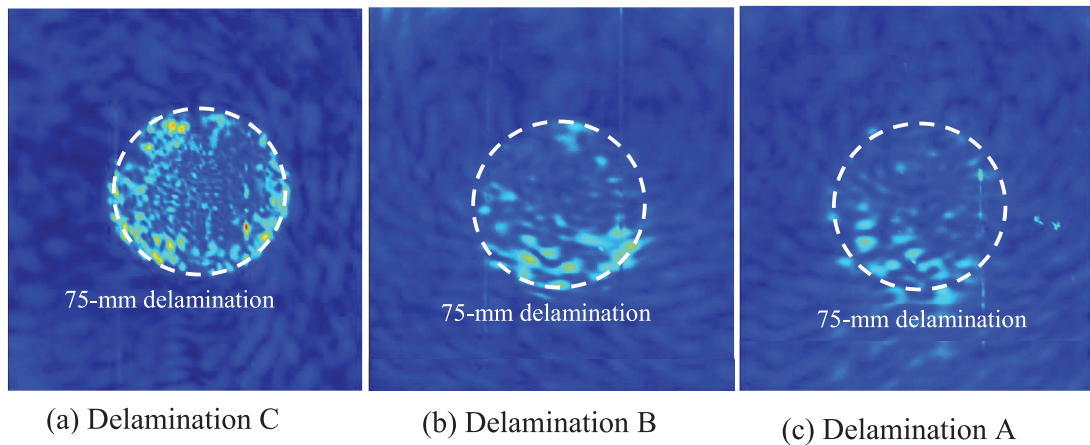


Figure 22. Energy distribution maps of the experimental wavefields of three scanning areas: (a) scanning area C, (b) scanning area B, and (c) scanning area A.

pristine line data. The time-space wavefield plot (Figure 23(a)) shows three guided modes, which are S0, A0, and SH0. The wavenumber spectrums of A0, S0, and SH0 agree well with analytical wavenumber curves, as shown in Figure 23(b). Figure 24(a), (c), and (e) show the time-space domains obtained from the linescan data of delaminations C, B, and A, respectively. We can clearly observe trapped waves, reflected waves, and transmitted waves in the delamination regions due to the interaction of guided waves with delaminations.

The delamination C has strongly trapped and reflected waves over the delamination region compared with the other two cases because it is close to the scanning surface (bottom surface). The time-space plot of delamination A shows slightly weak trapped waves over its delamination region compared with delamination B because it is far from the scanning surface. The experimental time-space plots showed excellent matching with numerical time-space plots (Figure 19). Figure 24(b), (d), and (f) shows wavenumber-frequency

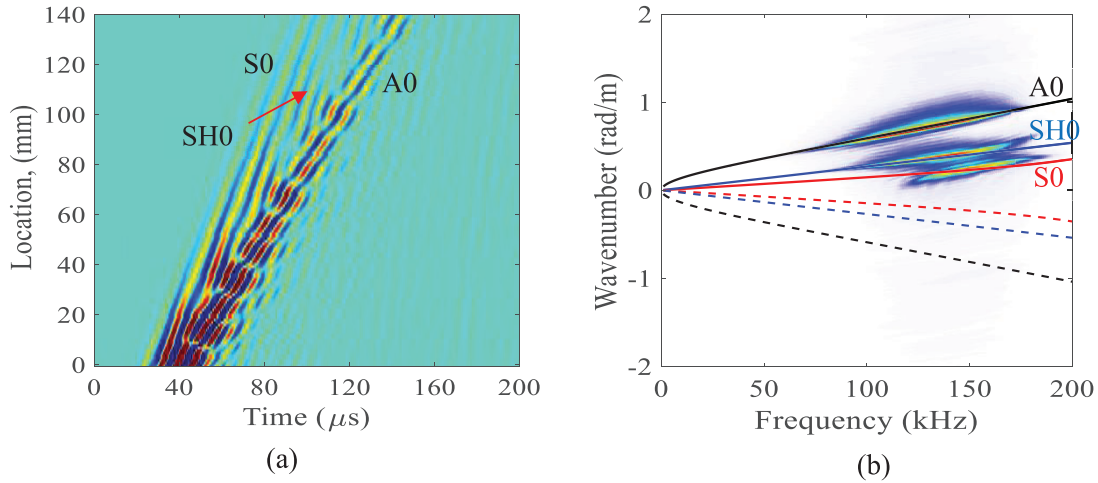


Figure 23. SLDV line scan of the pristine case: (a) time-space wavefield at 120 kHz and (b) wavenumber-frequency spectrum.

spectrums of delaminations C, B, and A, respectively. We can observe new wavenumber components in both positive and negative propagation sides, which are convenient with numerical results (Figure 19(b), (d), and (f)). These new components were generated due to the interaction of propagating guided waves with delaminations. We can remark that delamination C has strong and significant newly wavenumber components because it has strong trapped waves over its delamination region.

6. Summary, conclusion, and suggestions for future work

6.1. Summary

This article briefly presented three NDT, SHM, and SLDV experimental techniques. These techniques were used to detect, localize, and characterize three simulated delaminations inserted at different depths of a unidirectional composite plate. The first NDT experiment involved RollerFORM and OmniScan devices to localize and characterize the simulated delaminations by extracting A-scan plots, B-scan images, and C-scan images. We sufficiently explained the developed imaging method. The experimental SHM technique, in conjunction with the developed imaging method, was used to detect and quantify the interested delaminations. The experimental setup involves a network of twenty-two PWAS transducers to transmit guided waves and receive measured waves. The experiment involves pulse-echo and pitch-catch modes. The direction tuning and dispersion curves of the specimen test were presented. The scattered waves of sensing paths and the final images of multiple delaminations were determined. The effect of delamination depth on the scattered waves was studied. Multiphysics FEM simulations were implemented to study the Lamb waves propagating and

interaction with three simulated delaminations. The SLDV experiments were conducted to study the interaction of guided waves with delaminations and validate the numerical result. The numerical and experimental wavefield data of scanning areas were analyzed to study the interaction of Lamb waves with delaminations and quantify the interested delamination. The effect of delamination depth on the time-space wavefield and corresponding frequency-wavenumber spectrum was discussed. The numerical and experimental wavefield energy distribution maps were presented.

6.2. Conclusion

The Olympus RollerFORM can be used successfully to estimate the location, size, and depth of the delamination. The Lamb waves-based developed imaging method was successfully used to localize and size of the interested delaminations. This developed imaging method can be used to quantify delamination without setting a threshold value by using a combination of summation and multiplication imaging algorithms. The delamination depth can affect the energy of scattered waves. The near surface delamination has strong scattered waves compared with scattered waves of far surface delamination. Multiphysics FE simulations can be used sufficiently for visualizing the Lamb waves propagating and interaction with the structural delamination. The FE results show trapped waves over delaminations regions, which can be used to identify the location, size, and shape of delamination. The energy of trapped waves is affected by the delamination depth. The delamination, which is near the scanning surface, has strong and intensive trapped waves, while the delamination, which is far from the scanning surface, has weak and coarse trapped waves. A good agreement was achieved between the FE results and experimental SLDV results.

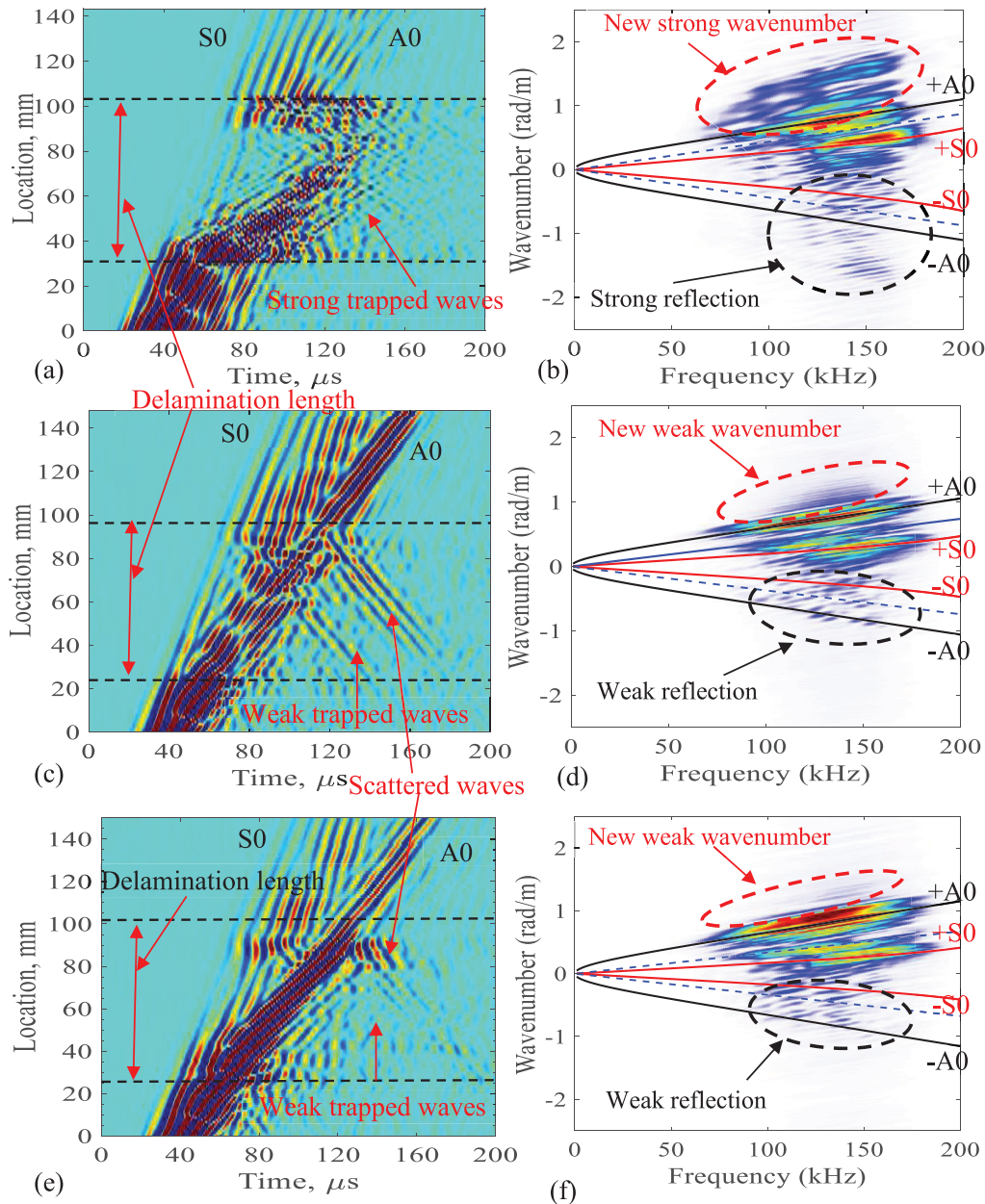


Figure 24. SLDV lines scan of delamination cases: (a, c, and e) time-space wavefield at 120 kHz of delaminations C, B, and A respectively, and (b, d, and f) wavenumber-frequency spectrum of delaminations C, B, and A respectively.

Both numerical and experimental wavenumber analysis results showed new wavenumber components due to trapped waves over delaminations regions. The energy distribution maps of numerical and experimental wavefields data can be used to quantify the structural delamination. Both numerical and experimental results demonstrated that the energy distribution over the delamination region could be affected by the delamination depth.

6.3. Future work

Further wavenumber analysis may be applied to the wavefield data to identify delamination. The developed

imaging method may be used for the sizing of actual fatigue cracks. A small fatigue crack can be sized using the developed imaging method.

Acknowledgements

This work was supported by Thi-Qar University (Iraq), and Laboratory for Active Materials and Smart Structures (LAMSS) are thankfully acknowledged.


Declaration of conflicting interests


The author(s) declared no potential conflicts of interest with respect to the research, authorship, and/or publication of this article.

Funding

The author(s) received no financial support for the research, authorship, and/or publication of this article.

ORCID iDs

Asaad Migot  <https://orcid.org/0000-0002-6760-7718>

Hanfei Mei  <https://orcid.org/0000-0002-8921-494X>

References

- Azuara G, Barrera E and Ruiz M (2018) Integration of algorithms for damage detection in thermoplastic materials inside electronic embedded devices. In: *9th European Workshop on Structural Health Monitoring Series (EWSHM 2018)*, Manchester, 10–13 July 2018.
- Giurgiutiu V (2014) *Structural Health Monitoring with Piezoelectric Wafer Active Sensors*. London: Academic Press Elsevier.
- Giurgiutiu V (2018) Predictive simulation of guide wave structural health monitoring in metallic and composite structures. In: *9th European Workshop on Structural Health Monitoring (EWSHM 2018)*. Manchester, 10–13 July 2018.
- Giurgiutiu V and Soutis C (2012) Enhanced composites integrity through structural health monitoring. *Applied Composite Materials* 19: 813–829.
- Gomes GF, Mendéz YA, Alexandrino PDSL, et al. (2018) The use of intelligent computational tools for damage detection and identification with an emphasis on composites – A review. *Composite Structures* 196: 44–54.
- Haider MF, Migot A, Bhuiyan MY, et al. (2018) Experimental investigation of impact localization in composite plate using newly developed imaging method. *Inventions* 3(3): 59.
- Hayashi T and Kawashima K (2002) Multiple reflections of Lamb waves at a delamination. *Ultrasonics* 40(1–8): 193–197.
- He J, Ran Y, Liu B, et al. (2017) A fatigue crack size evaluation method based on Lamb wave simulation and limited experimental data. *Sensors* 17(9): 2097.
- He MY and Hutchinson JW (1989) Damage detection in composite materials using frequency response methods. *Journal of Applied Mechanics* 111(1): 270–278.
- Ihn JB and Chang FK (2008) Pitch-catch active sensing methods in structural health monitoring for aircraft structures. *Structural Health Monitoring* 7(1): 5–19.
- Juarez PD and Leckey C (2016) Detection of manufacturing defects via wavefield image processing techniques: an experimental study. In: *43rd Annual review of progress in quantitative non-destructive evaluation*, Atlanta, GA, 17–22 July 2016, p.142.
- Mei H and Giurgiutiu V (2018) Predictive 1D and 2D guided-wave propagation in composite plates using the SAFE approach. In: *Proceedings of the SPIE health monitoring of structural and biological systems XII*, Denver, CO, 27 March, paper no. 106000P.
- Mei H and Giurgiutiu V (2019a) Guided wave excitation and propagation in damped composite plates. *Structural Health Monitoring* 18(3): 690–714.
- Mei H and Giurgiutiu V (2019b) Wave damage interaction in metals and composites. In: *Proceedings of the SPIE health monitoring of structural and biological systems XII*, Denver, CO, 27 March, paper no. 1097200.
- Mei H, Haider MF, Joseph R, et al. (2019a) Recent advances in piezoelectric wafer active sensors for structural health monitoring applications. *Sensors* 19: 383.
- Mei H, Migot A, Haider MF, et al. (2019b) Vibration-based in-situ detection and quantification of delamination in composite plates. *Sensors* 19: 1734.
- Mei H, Yuan S, Qiu L, et al. (2016) Damage evaluation by a guided wave-hidden Markov model based method. *Smart Materials and Structures* 25: 025021.
- Mesnil O, Leckey CAC and Ruzzene M (2014) Instantaneous and local wavenumber estimations for damage quantification in composites. *Structural Health Monitoring* 14(3): 193–204.
- Michaels JE and Michaels TE (2007) Guided wave signal processing and image fusion for in situ damage localization in plates. *Wave Motion* 44(6): 482–492.
- Michaels JE, Michaels TE and Ruzzene M (2011) Frequency-wavenumber domain analysis of guided wavefields. *Ultrasonics* 51(4): 452–466.
- Migot A, Bhuiyan Y and Giurgiutiu V (2019) Numerical and experimental investigation of damage severity estimation using Lamb wave-based imaging methods. *Journal of Intelligent Material Systems and Structures* 30(4): 618–635.
- Migot A, Bhuiyan Y and Giurgiutiu V (2020) Impact localization on composite plates using two developed imaging methods. In: *Proceedings of the SPIE active and passive smart structures and integrated systems XIV*, California, United States, 22 April, paper no. 113760V.
- Migot A and Giurgiutiu V (2017) Impact localization using sparse PWAS networks and wavelet transform. In: *11th International workshop on structural health monitoring*, Stanford, CA, 12–14 September 2017, pp.391–398.
- Olympus (2018) *RollerFORM Specifications*. Available at: <https://www.olympus-ims.com/en/rollerform/> (accessed 15 December 2018).
- Park B, An YK and Sohn H (2014) Visualization of hidden delamination and debonding in composites through non-contact laser ultrasonic scanning. *Composites Science and Technology* 100: 10–18.
- Radziński M, Kudela P, Ostachowicz W, et al. (2020) Lamb-wave-based method in the evaluation of self-healing efficiency. *Applied Sciences* 10(7): 2585.
- Ruzzene M (2007) Frequency – wavenumber domain filtering for improved damage visualization. *Smart Materials and Structures* 16: 2116–2129.
- Shen Y and Cesnik CES (2016) Hybrid local FEM/global LISA modeling of damped guided wave propagation in complex composite structures. *Smart Materials and Structures* 25(9): 20.
- Shen Y and Giurgiutiu V (2015) Effective non-reflective boundary for Lamb waves: Theory, finite element implementation, and applications. *Wave Motion* 58: 22–41.
- Su Z, Cheng L, Wang X, et al. (2009) Predicting delamination of composite laminates using an imaging approach. *Smart Materials and Structures* 18(7): 74002–74010.
- Su Z, Ye L and Lu Y (2006) Guided Lamb waves for identification of damage in composite structures: A review. *Journal of Sound and Vibration* 295(3–5): 753–780.

- Tian Z, Leckey C, Rogge M, et al. (2013) Crack detection with Lamb wave wavenumber analysis. In: *Proceedings of SPIE, health monitoring of structural and biological systems*, San Diego, CA, 17 April, vol. 8695, p.86952Z. Bellingham, WA: SPIE.
- Tian Z, Leckey C, Yu L, et al. (2015) Impact induced delamination detection and quantification with guided wavefield analysis. In: *Proceedings of SPIE sensors and smart structures technologies for civil, mechanical, and aerospace systems*, San Diego, CA, 3 April, paper no. 94351P.
- Wang C H, Rose JT and Chang F-K (2004) A synthetic time-reversal imaging method for structural health monitoring. *Smart Materials and Structures* 13(2): 415–423.
- Yu L and Giurgiutiu V (2010) Piezoelectric wafer active sensor guided wave imaging. In: *Proceedings of SPIE smart sensor phenomena, technology, networks, and systems*, San Diego, CA, 3 April, paper no.76480S.
- Zou Y, Tong L and Steven G P (2000) Vibration-based model-dependent damage (delamination) identification and health monitoring for composite structures - a review. *Journal of Sound and Vibration* 230(2): 357–378.